

Magnetic proximity-induced magnetoresistance in $Pt/Tm_3Fe_5O_{12}$ heterostructures

Zhengguo Liang(梁正国), Kunjie Dai(戴坤杰), Qiming Lv(吕崎鸣), Ao Wang(王傲), Jinfeng Zhang(章金凤), and Lingfei Wang(王凌飞)

Citation: Chin. Phys. B, 2026, 35 (**7**): 077512. DOI: 10.1088/1674-1056/ae5788
http://cpb.iphy.ac.cn; http://iopscience.iop.org/cpb

What follows is a list of articles you may be interested in

Controlling tilted chiral magnetic textures in Janus Nb*X*Te (*X* = Se, S) monolayers via magnetic field and strain engineering

Xiao-Bo Yu(于晓波), Dong Fan (范栋), and Chang-Wen Zhang(张昌文)
Chin. Phys. B, 2026, 35 (**3**): 037504. DOI: 10.1088/1674-1056/ae3c8a

Thickness dependence of the magnetic properties of barium ferrite films prepared by pulsed laser deposition

Chengbo Zhao(赵诚博), Bowei Han(韩博纬), Yuchen Zhao(赵宇辰), Yang Sun(孙洋), Lichen Wang(王利晨), Ruoshui Liu(刘若水), Yunzhong Chen(陈允忠), and Dengjing Wang(王登京)
Chin. Phys. B, 2026, 35 (**2**): 027504. DOI: 10.1088/1674-1056/adf6a5

Temperature-dependent magnetotransport properties of $CoFe_2O_4$/Pt heterostructure

Haomang He(何浩茫), Ruijie Xu(徐睿劼), Anke Song(宋安柯), Zhongqiang Chen(陈中强), and Xuefeng Wang(王学锋)
Chin. Phys. B, 2026, 35 (**1**): 017502. DOI: 10.1088/1674-1056/ae181c

CrAlGe: An itinerant ferromagnet with strong tunability by heat treatment

Zhaokun Dong(董昭昆), Zhen Wang(王振), Te Zhang(张特), Junsen Xiang(项俊森), Shuai Zhang(张帅), Lihua Liu(刘丽华), and Peijie Sun(孙培杰)
Chin. Phys. B, 2022, 31 (**11**): 117502. DOI: 10.1088/1674-1056/ac7858

Origin of itinerant ferromagnetism in two-dimensional Fe_3GeTe_2

Xi Chen(陈熙), Zheng-Zhe Lin(林正喆), and Li-Rong Cheng(程丽蓉)
Chin. Phys. B, 2021, 30 (**4**): 047502. DOI: 10.1088/1674-1056/abd164

RAPID COMMUNICATION

Magnetic proximity-induced magnetoresistance in $Pt/Tm_3Fe_5O_{12}$ heterostructures

Zhengguo Liang(梁正国), Kunjie Dai(戴坤杰), Qiming Lv(吕崎鸣), Ao Wang(王傲), Jinfeng Zhang(章金凤), and Lingfei Wang(王凌飞)†

Hefei National Research Center for Physical Sciences at Microscale, University of Science and Technology of China, Hefei 230026, *China*

(Received 13 February 2026; revised manuscript received 24 March 2026; accepted manuscript online 26 March 2026)

Thin Pt films on magnetic garnet exhibit ferromagnetic-like transport properties, which may affect the functionality of Pt in spin current detection, although direct observation of this effect has not been made. Here, we report the observation of a magnetic proximity-induced magnetoresistance (MP-MR) in $Pt/Tm_3Fe_5O_{12}$ (TmIG) heterostructures. This electrical signal is directly correlated with the itinerant ferromagnetism induced by the magnetic proximity effect (MPE) at the Pt/TmIG interface. The existence of MP-MR has been unambiguously verified through the insertion of a Cu interlayer and supported by quantitative analysis, which also enables clear differentiation from the spin Hall magnetoresistance (SMR) signal. The weak ferromagnetism observed in Pt follows the typical behavior of itinerant ferromagnetism, as predicted by the Stoner criterion. By utilizing TmIG films with enhanced perpendicular magnetic anisotropy (PMA), we achieve amplification of the MP-MR effect. Our results demonstrate that the magnitude of MP-MR increases with decreasing temperature. Moreover, the strength of MP-MR can be substantially enhanced through improved PMA in TmIG. These findings underscore the potential of MPE-based magnetotransport phenomena for advancing spintronic device applications.

Keywords: magnetic proximity effect, magnetic garnet, itinerant ferromagnetism, perpendicular magnetic anisotropy

PACS: 75.47.–m

DOI: 10.1088/1674-1056/ae5788 **CSTR:** 32038.14.CPB.ae5788

1. Introduction

Magnetic phenomena arising at the nonmagnetic/ferromagnetic (NM/FM) heterostructures have attracted significant research interest over the past decades.[1–6] A variety of novel physical effects have been observed in these systems, such as the spin Seebeck effect (SSE),[2] the unidirectional spin Hall magnetoresistance (USMR),[5] and the spin-orbit torque (SOT).[6] The physical interpretations of these phenomena are mostly based on a combination of the spin Hall effect (SHE) and interface-related mechanisms. Specifically, at the NM/FM heterointerfaces, the nonlocal exchange coupling can extend from the FM layer into the NM layer and induce an additional magnetic moment in the interfacial region of the NM layer, leading to the so-called magnetic-proximity effect (MPE).[7,8] The MPE can give rise to novel transport phenomena in non-magnetic materials. For instance, the quantum anomalous Hall effect (QAHE) has been observed in graphene and topological insulators grown on magnetic garnet films.[9–14]

Bilayer heterostructures consisting of garnet-structured ferrite and nonmagnetic metal Pt provide an excellent platform for investigating the MPE. Pt is close to the Stoner criterion and has been shown to exhibit ferromagnetic ordering when grown on a magnetic substrate.[15] Garnet-structured ferrite is a typical ferrimagnetic insulator with a high Curie temperature exceeding 500 K, and its highly insulating nature enables a deterministic characterization of potential magnetotransport properties in the Pt layer. A growing body of experimental evidence suggests that MPE may indeed exist in such systems. Huang *et al.* suggested that MPE may play a role in triggering a hybrid magnetoresistance at the $Pt/Y_3Fe_5O_{12}$ (YIG) interface.[16–18] The SSE signal could comprise contributions from both the intrinsic SSE and the anomalous Nernst effect (ANE) if MPE is present at the Pt/YIG interface.[19,20] Moreover, x-ray magnetic circular dichroism (XMCD) is widely regarded as an effective technique for studying MPE, yet recent XMCD measurements have yielded controversial results regarding the presence of MPE in the Pt/YIG system.[21,22] Recent studies have revealed a range of intriguing physical phenomena in $Pt/Tm_3Fe_5O_{12}$ (TmIG) heterostructures, including SOT-induced magnetization switching,[6,23] current-induced chiral domain wall motion,[24,25] interfacial Dzyaloshinskii–Moriya interaction (DMI),[24–26] and topological Hall effects.[27–29] These effects may arise from a competitive mechanism between SHE and MPE in Pt/TmIG, where the interplay between these two effects governs the sign and amplitude of the AHE.[30–32] Despite the abundance of physical phenomena stimulated by MPE, its direct observation remains challenging.

†Corresponding author. E-mail: wanglf@ustc.edu.cn

© 2026 Chinese Physical Society and IOP Publishing Ltd. All rights, including for text and data mining, AI training, and similar technologies, are reserved.

For example, MPE has not been independently observed in studies of both SSE[19,20] and AHE.[30–32] Therefore, developing a reliable experimental approach for the direct observation of MPE in NM/FM heterostructures is crucial for advancing the exploration of spintronic phenomena and devices.

In this work, we observed an intriguing magnetoresistance (MR) that is directly correlated to the MPE in Pt/TmIG heterostructures, named the MP-induced MR (MP-MR). At the Pt/TmIG interface, the MPE-induced itinerant ferromagnetism in the Pt interfacial layer can cause additional spin-dependent scattering of electrons, thus resulting in the MP-MR. Since the MP-MR is insensitive to the spin current injected into Pt, it can be easily distinguished from the spin Hall magnetoresistance (SMR) by introducing a Cu interlayer with variable thickness. By utilizing TmIG films with stronger perpendicular magnetic anisotropy (PMA), we achieved an enhancement of MP-MR by 40% at 100 K. Our study of MP-MR has provided crucial evidence for the existence of MPE at the Pt/garnet interface. Furthermore, based on the control of MP-MR, it introduces a new approach for regulating MPE, holding potential for practical spintronic applications.

2. Results and discussion

Structural and magnetic characterization High-quality epitaxial TmIG films with robust PMA were deposited on (111)-oriented gadolinium gallium garnet ($Gd_3Ga_5O_{12}$, GGG) substrates by pulsed laser deposition (PLD). The growth condition optimization for high-quality TmIG films has been previously reported.[33] We first measured the magnetic field-dependent magnetization (M–H) hysteresis loops of TmIG/GGG(111) films from 300 K to 100 K (Fig. 1(a)). The M–H curves measured with the out-of-plane magnetic field ($H_\perp$) exhibit well-defined hysteresis loops as typical ferromagnets or ferrimagnets, ensuring an excellent PMA within the temperature (T) range we studied. The saturation magnetization (M_s) and coercive field (H_c), extracted from the loops, are plotted in Figs. 1(b) and 1(c) as a function of T. The M_s initially maintains a nearly constant value of $\sim$ 100 emu/cm^3 above 200 K and decreases to 78 emu/cm^3 upon cooling down to 100 K. The decrease of M_s is also accompanied by a gradual increase of H_c from 0.92 Oe (at 200 K) to 60 Oe (at 100 K). In fact, TmIG consists of three magnetic sublattices: an octahedral Fe sublattice (a sites), a tetrahedral Fe sublattice (d sites), and a dodecahedral Tm sublattice (c sites), which is shown in the illustration of Fig. 1(b). The two Fe sublattices can be treated as a single effective Fe magnetic sublattice due to their strong antiferromagnetic superexchange interaction.[34] The magnetic moment of Tm^{3+} ions is more sensitive to T than that of Fe^{3+} ions. As T decreases, the net magnetic moment of Tm^{3+} ions increases at a faster rate than that of Fe^{3+} ions, leading to the reduction of net moment in the TmIG unit cell. This is a typical phenomenon for a ferrimagnet when T approaches the compensation point, which is defined as the T where the magnetic moments of the two magnetic sublattices cancel out.[35,36] The non-zero M_s values of these M–H curves confirm that the TmIG/GGG(111) films do not experience any compensation point within the T range studied.[37,38] In brief, our TmIG/GGG(111) film maintains a relatively large M_s between 100 K and 300 K with no compensation point and preserves good PMA, which makes it an excellent platform for studying MPE.

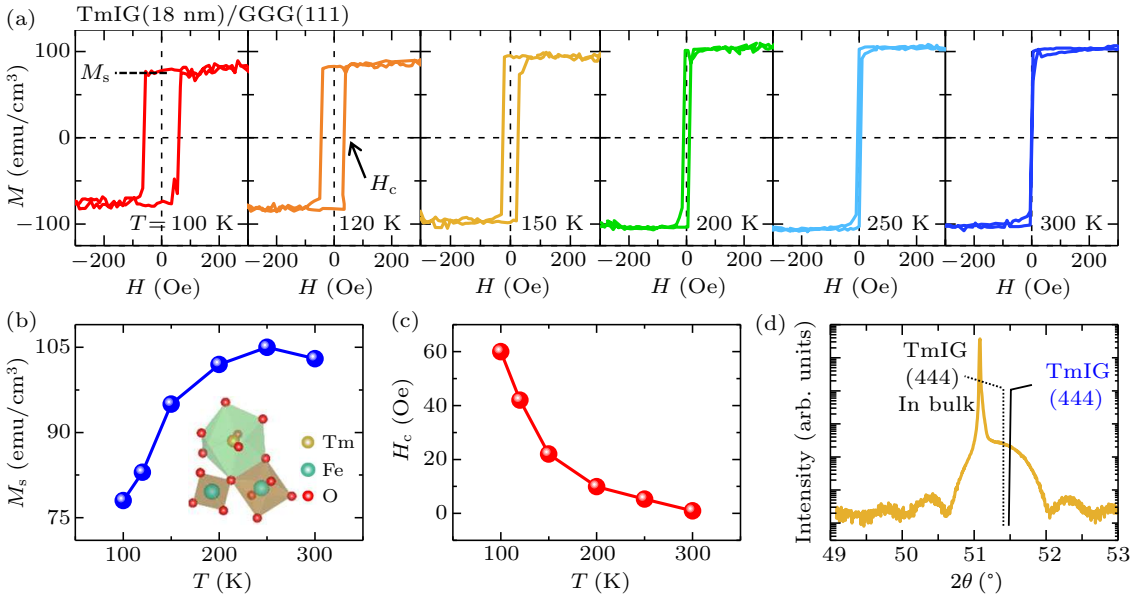


Fig. 1. Structural and magnetic characterization of $Tm_3Fe_5O_{12}/Gd_3Ga_5O_{12}(111)$ [TmIG/GGG(111)] thin films. (a) Magnetic field-dependent magnetization (M–H) hysteresis loops measured from 300 K to 100 K. All the M–H loops are measured with H applied along the film normal ($H_\perp$). (b) and (c) T versus magnetic parameters extracted from the M–H loops, including (b) saturated magnetization (M_s) and (c) coercive field (H_c). A schematic illustration of the three magnetic sublattices of TmIG is provided in the inset of (b). (d) X-ray diffraction (XRD) 2θ–ω linear scans of TmIG (18 nm)/GGG(111) films.

Consistent with the robust ferrimagnetism and PMA, the TmIG films also exhibit high epitaxial quality. As shown in Fig. 1(d), the x-ray diffraction (XRD) 2θ–ω linear scan of an 18 nm-thick TmIG/GGG(111) epitaxial film displays well-defined TmIG(444) diffraction peaks and sharp Laue fringes, indicating sharp film/substrate interfaces. The film thickness determined by Laue fringes is 18 nm. For performing the subsequent electrical transport measurements, we further deposited a 5 nm-thick Pt layer on top of the TmIG thin film using PLD. The thickness of the Pt layer was determined by fitting the x-ray reflectivity (XRR) curve (Fig. S1).

The coexistence of SMR and MP-MR in Pt/TmIG heterostructures Before exploring the MP-MR, we first consider the competing effect, the SMR. SMR has been widely used to detect the spin transport parameters at the interface between a magnetic insulator (MI) and a transition heavy metal (HM).[39] In the HM/MI bilayer, a charge current ($\boldsymbol{j}$) injected into the HM layer generates a transverse spin current ($\boldsymbol{j}_s$) towards the HM/MI interface, thus simulating the SHE. The $\boldsymbol{j}_s$ can be expressed by the following equation:

$$\boldsymbol{j}_s = \theta_{SH}(\boldsymbol{j} \times \boldsymbol{\sigma}),$$

where θ_{SH} represents the spin Hall angle (SHA) of the HM, and $\boldsymbol{\sigma}$ represents the spin polarization. An accumulation of spins can occur at the interface, generating a diffusion spin current that flows opposite to the SHE-induced spin current, which can be converted into an additional $\boldsymbol{j}$ via the inverse SHE to reduce the resistance. When $\boldsymbol{\sigma}$ is parallel to M of the MI, spin accumulation is not suppressed, resulting in the lowest resistance. Conversely, when $\boldsymbol{\sigma}$ is perpendicular to M of the MI, spin accumulation is reduced due to spin-transfer torque, leading to the highest resistance. The corresponding resistance change in the HM is referred to as the SMR, which is considered an interface effect, depending only on the relative orientation of the $\boldsymbol{\sigma}$ and the M at the contact.[39] To extract the SMR signal, we rotate the H vector along three axes: 1) x axis: the direction of the $\boldsymbol{j}$ vector; 2) y axis: in-plane axis perpendicular to the $\boldsymbol{j}$ vector (the direction of the $\boldsymbol{\sigma}$ vector due to SHE); 3) z axis: along the film normal. And we define the angle between the H vector and the x, y, and z axes as α, β, and γ, respectively. We set $\mu_0 H = 1$ T to fully align M along the H vector and then measured the resistance (R). The SMR value is calculated by $R_{SMR} = [R(\alpha,\ \beta;\ \text{or}\ \gamma) - R(\alpha,\ \beta;\ \text{or}\ \gamma = 90°)]/R(\alpha,\ \beta;\ \text{or}\ \gamma = 90°)$. Figure 2(a) shows α, β, and γ-dependent R_{SMR} of the Pt(5 nm)/TmIG(18 nm) sample. As H rotates along the x and z axes, both the R_{SMR}–α and R_{SMR}–β curves exhibit a typical sinusoidal line shape. And the maximum value of R_{SMR} for both cases can reach 0.015%, which is comparable to the reported values observed at the Pt/YIG interface.[40] By contrast, as H rotates along the y axis, the $H \perp \sigma$ relationship prevails, leading to $R_{SMR} = 0$ for all the γ values.

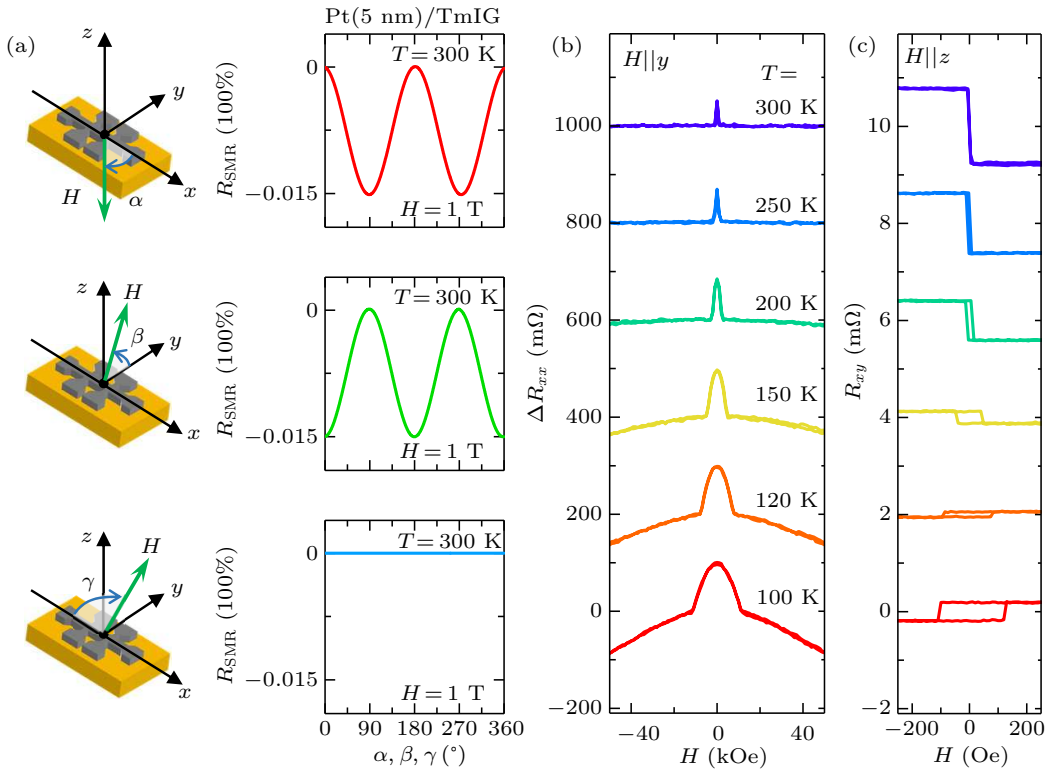


Fig. 2. The coexistence of the spin Hall magnetoresistance (SMR) and magnetic proximity effect-induced magnetoresistance (MP-MR) in Pt/TmIG. (a) SMR measurement of the Pt/TmIG. $R_{SMR} = [R(\alpha,\beta,\text{or}\ \gamma) - R(\alpha,\beta,\text{or}\ \gamma = 90°)]/R$ (α, β, or $\gamma = 90°$). And H strength is set to be 1 T, which is high enough to fully align M with H. (b) H-dependent longitudinal resistance (R_{xx}) of the Pt/TmIG sample at 300 K to 100 K. ΔR_{xx} is defined as $\Delta R_{xx} = R_{xx}(H) - R_{xx}(H = H_s)$ for the Pt(5 nm)/TmIG(18 nm) sample. H was applied parallel to the y-axis. (c) H-dependent transverse Hall resistance (R_{xy}) of Pt/TmIG measured at various T. H was applied parallel to the z-axis.

After conducting the standard SMR characterizations, we measured the H-dependent longitudinal resistance (R_{xx}) and transverse Hall resistance (R_{xy}) from the Pt/TmIG samples. Figure 2(b) presents the resistance change (ΔR_{xx}) as a function of H applied along the y-axis for the Pt/TmIG sample at 300 K to 100 K. ΔR_{xx} is defined as $\Delta R_{xx} = R_{xx}(H) - R_{xx}(H = H_s)$ for the Pt(5 nm)/TmIG(18 nm) sample. For $T > 200$ K, ΔR_{xx} decreases with increasing H and remains nearly constant above H_s, which is consistent with SMR theory.[40] At $T > 200$ K, ΔR_{xx} decreases gradually as H increases at $H < H_s$ and reaches the zero value at $H \geq H_s$, which is consistent with a typical SMR behavior. At $T \leq 200$ K, in addition to the SMR peak at $H < H_s$, ΔR_{xx} decreases continuously as H exceeds H_s, signifying an additional MR contribution. Unlike the typical SMR, this negative MR is not sensitively correlated with the direction of M in TmIG.[41,42] Figure 2(c) shows the R_{xy}–H hysteresis loops of Pt/TmIG heterostructures measured at various T. Upon cooling, the saturation value of R_{xy} decreases first ($T \geq 120$ K) and then increases ($T < 120$ K), accompanied by a sign change of R_{xy} from negative to positive. The unusual evolutions of ΔR_{xx} and R_{xy} at $T < 150$ K suggest that they may share similar origins.

In Pt/TmIG heterostructures, R_{xy} primarily arises from the SHE and MPE. The former mainly results from the accumulation of $\boldsymbol{j}_s$ at the Pt/TmIG interface, while the latter originates from the ferromagnetism of Pt induced by MPE.[31,32] At $T \geq 150$ K, the SHE-induced negative AHE dominates the R_{xy}, but its magnitude gradually decreases upon cooling. Meanwhile, the MPE-induced positive AHE progressively increases as T decreases, due to the strengthening of exchange coupling between the Fe^{3+} 3d orbitals and the Pt 5d orbitals. Therefore, at low $T < 150$ K, the MPE-induced positive AHE dominates the R_{xy}. On this basis, this R_{xy} sign change can be well explained by the competition between SHE and MPE at the Pt/TmIG heterointerface.[31,32] Since the emergence of a negative MR signal is always accompanied by the sign reversal of R_{xy}, we suggest that the negative MR effect likely originates from the MPE.

The origin of MP-MR in Pt/TmIG heterostructures

To clarify the physical origin of the observed unusual MR, we inserted thin Cu layers with variable thickness (t_{Cu}) at the Pt/TmIG interface and measured the ΔR_{xx}–H curves (Figs. 3(a) and 3(b)). Since Cu is an effective spin conductor with a long spin diffusion length (~ 350 nm), a few nanometers thick Cu layer should not significantly suppress the spin current.[30] Additionally, the electronic structure of Cu is far from the Stoner instability, meaning the nonlocal exchange interaction cannot extend over such a thickness and stimulate the MPE.[30] Figure 3(a) presents the ΔR_{xx}–H curve measured from a Pt/Cu/TmIG/GGG(111) sample with H applied parallel to the y-axis. The insertion of a Cu spacer above TmIG leads to a slight suppression of the SMR magnitude (Fig. S2). More importantly, the negative MR behavior observed in Pt/TmIG is significantly suppressed. In the Pt/Cu(1 nm)/TmIG film, we find that the negative MR behavior only becomes apparent when the T drops below 120 K. For samples with a t_{Cu} greater than 1 nm, ΔR_{xx} exhibits typical SMR behavior as a function of H within the T range we studied (Figs. 3(a) and S2). Based on these findings, we have strong evidence to conclude that the new MR effect we observed originates from the MPE, which we define as MP-MR.

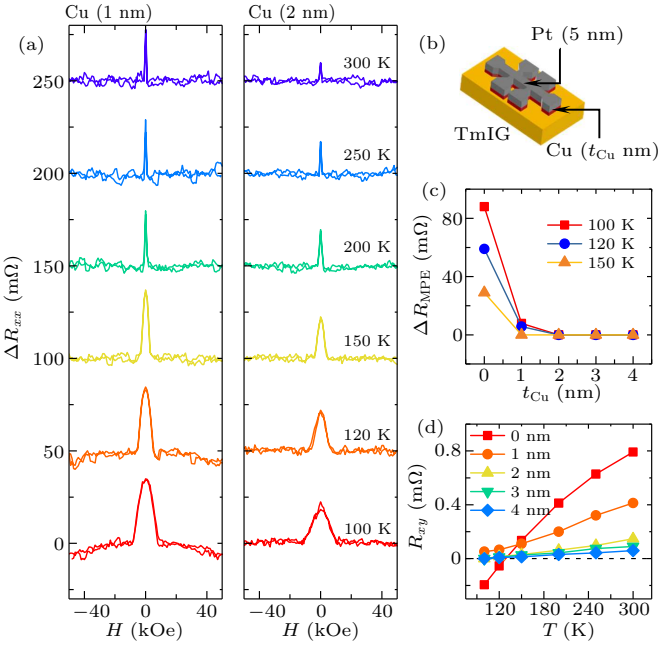


Fig. 3. Transport measurements for the Pt/Cu/TmIG sample. (a) H-dependent transport measurements for the Pt/Cu(1–2 nm)/TmIG sample at 300 K to 100 K. (b) Schematics of the Pt(5 nm)/Cu(t_{Cu} nm)/TmIG heterostructure. (c) Cu thickness (t_{Cu}) dependence of ΔR_{MPE} for Pt(5 nm)/Cu(t_{Cu} nm)/TmIG heterostructure at 150 K to 100 K. $\Delta R_{MPE} = -\Delta R_{xx}(H = 5\ \text{T})$. (d) R_{xy} for Pt/TmIG and Pt/Cu(t_{Cu})/TmIG as a function of T.

To quantitatively study MP-MR, we define $\Delta R_{MPE} = -\Delta R_{xx}(\mu_0 H = 5\ \text{T})$ and plot the t_{Cu}-dependent ΔR_{MPE} in Fig. 3(c) (see Figs. S2 and S3 for details). At 120 K and 100 K, as t_{Cu} increases, ΔR_{MPE} is dramatically suppressed at $t_{Cu} = 1$ nm, and it reaches 0 for $t_{Cu} > 2$ nm. At 150 K, the t_{Cu}-induced suppression of ΔR_{MPE} becomes even stronger. A 1 nm-thick Cu layer is enough to fully suppress MP-MR. The Cu spacer-modulated MPE can be further verified by R_{xy}–T curves summarized in Fig. 3(d). A different T dependence of R_{AHE} is observed in Pt/TmIG and Pt/Cu/TmIG. The decrease in R_{AHE} for Pt/TmIG is faster than that for Pt/Cu/TmIG, and the competition between the MPE and SHE leads to a sign change near 120 K. For the samples of Pt/Cu(1–5 nm)/TmIG, the Cu layers isolate the Pt/TmIG layers, suppressing the MPE. As a result, the R_{AHE} of Pt/Cu/TmIG continues to decrease as T decreases, exhibiting similar behavior to the dependence of M_s (Fig. 1(b)), and no sign change occurs. Furthermore, the introduction of the Pt/Cu interface and the current shunting effect caused by the Cu layers lead to a reduction

in the overall $R_{\rm AHE}$ value.[32,39,43] The above analysis further confirms that the measured ΔR_{xx} in Pt/TmIG includes contributions from both SMR and MP-MR.

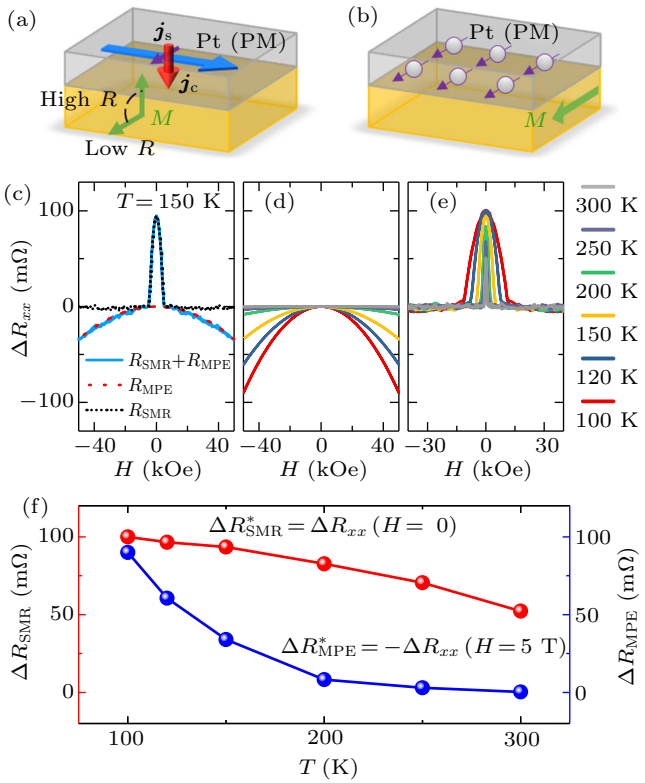


Fig. 4. The origin of MP-MR in Pt/TmIG heterostructures. (a) and (b) Schematics for the mechanisms of the origin of SMR and MP-MR in Pt/TmIG. (c) The experimental data of ΔR_{xx} in Pt/TmIG as a function of the H at 150 K and the fitting curve with the quadratic functions. The fitting results align well with the experimental data, and by subtracting the MP-MR signal obtained from the fitting, we can isolate the pure SMR signal. (d) The MP-MR curve of Pt/TmIG at different T. (e) The SMR curve of Pt/TmIG at different T after subtracting the MP-MR signal, all of which conform to the typical SMR characteristics. (f) $\Delta R^*_{\rm SMR}$ and $\Delta R^*_{\rm MPE}$ for Pt/TmIG as a function of T. $\Delta R^*_{\rm MPE} = -\Delta R_{xx}(H = 5\ {\rm T})$ and $\Delta R^*_{\rm SMR} = \Delta R_{xx}(H = 0)$.

To precisely determine the magnitude of MP-MR in Pt/TmIG, we attempt to discuss and clarify the physical origins of both SMR and MP-MR. SMR is a nonequilibrium proximity effect, which makes the electrical transport of the metal film strongly coupled to the magnetic properties of the adjacent insulating ferrimagnet (Fig. 4(a)).[39] When applying a $\boldsymbol{j}$ along the Pt layer within the xy plane, the SHE generates a y-axis-polarized $\boldsymbol{j}_{\rm s}$ flowing in the z direction, thereby creating spin accumulations at the Pt/TmIG and vacuum/Pt interfaces. When M of the TmIG is aligned with the y axis ($M \parallel y$), the interface $\boldsymbol{j}_{\rm s}$ vanishes (as it does at the vacuum interface), leading to a low $R_{\rm SMR}$. When M of the TmIG is aligned with the z axis ($M \parallel z$), the accumulated spins are partially absorbed at the interface and dissipated as a spin-transfer torque to M, modulating the $\boldsymbol{j}_{\rm s}$ distribution in Pt, resulting in high resistance for $R_{\rm SMR}$.[39] In our study, $\Delta R_{\rm SMR} = R_{xx}(M \parallel z) - R_{xx}(M \parallel y)$. In Pt/TmIG, the interface exchange coupling between the electron spins in Pt and Fe plays a significant role in the MPE within Pt (Fig. 4(b)). TmIG has strong PMA, and its orbital hybridization with Pt is sufficient to induce a stronger exchange coupling compared to Pt/YIG. As a result, Pt may satisfy the Stoner criterion, acquiring itinerant ferromagnetism, as previously demonstrated in both theoretical and experimental studies.[44–46] In an itinerant ferromagnet, the magnetism does not arise from localized atomic magnetic moments but from the spin polarization of itinerant electrons themselves. In a relatively large H range, the spin polarization (P) of itinerant electrons increases linearly with H. As P increases, the probability of electron spin-flip scattering significantly decreases. Consequently, R continuously decreases with increasing H (negative MR), without exhibiting saturation at high fields.[44–46] The R–H relationship can be well-fitted by a power law ($R \propto H^2$), which is a typical feature of itinerant ferromagnetism.[47–49] By subtracting the MP-MR quadratic MR contribution (Figs. 4(c), S4, and Table S1), we can isolate the pure SMR signal. Figures 4(d) and 4(e) show the MP-MR curve of Pt/TmIG and the SMR contribution to its ΔR_{xx} at different T, respectively. Based on these data, we obtain $\Delta R^*_{\rm MPE} = -\Delta R_{xx}(H = 5\ {\rm T})$ and $\Delta R^*_{\rm SMR} = \Delta R_{xx}(H = 0)$, as presented in Fig. 4(f). As T decreases, both $\Delta R_{\rm SMR}$ and $\Delta R_{\rm MPE}$ increase. So far, we have successfully isolated the SMR and MP-MR signals in Pt/TmIG and determined their respective T dependencies.

PMA enhancement of MP-MR Based on the origin of the MP-MR discussed above, our analysis suggests that optimizing PMA to enhance the MPE may serve as a potential approach for improving MP-MR. To enhance the PMA of TmIG films, we grew Pt/TmIG films on (111)-oriented $Gd_{2.6}Ca_{0.4}Ga_{4.1}Mg_{0.25}Zr_{0.65}O_{12}$ [SGGG(111)] and $Gd_3Sc_2Ga_3O_{12}$ [GSGG(111)] substrates. These substrates have larger lattice constants than TmIG and GGG, thus imposing larger tensile strain on the TmIG(111) films.[50] As shown in Fig. S5, all of the curves display well-defined (444) diffraction peaks and sharp Laue fringes, indicating sharp film/substrate interfaces. Both the in-plane and out-of-plane M–H hysteresis loops (Figs. 5(a)–5(c)) further confirm the enhanced PMA in these tensile-strained TmIG films. Figures 5(d)–5(f) present the ΔR_{xx}–H at 150 K for the Pt/TmIG sample grown on different substrates. Since SMR for hard axes shows a continuous evolution with H until M is saturated at the effective anisotropy field $H_{\rm s}$, the $H_{\rm s}$–T curves of Pt/TmIG on different substrates are extracted in Fig. 5(g).[51] We found that the enhancement of $H_{\rm s}$ can be achieved by changing the substrate at a constant T, while $H_{\rm s}$ for TmIG on the same substrate increases as T decreases (Figs. S6 and S7). Therefore, we suggest that the increment of MP-MR upon cooling is partially due to the enhancement of PMA.

To better understand the relationship between PMA and MP-MR, values of $\Delta R^*_{\rm MPE}$ were calculated for these TmIG

films and plotted as functions of $K_\perp$ and $K_\perp = H_s \cdot M_s/2$ (see Figs. 5(h) and S7). MP-MR not only increases as T decreases, as reported in previous studies, but can also be significantly enhanced by increasing PMA. For Pt/TmIG on the GGG substrate, ΔR^*_{MPE} increased from 0.36 mΩ to 89.9 mΩ as T decreased. For Pt/TmIG on the GSGG substrate, ΔR^*_{MPE} increased from 5.1 mΩ to 125.6 mΩ as T decreased, demonstrating the effectiveness of stronger PMA in enhancing MPE. Our observations provide direct evidence of the correlation between PMA and MPE, which has been previously suggested in the literature.[9–14] Notably, as shown in Fig. 5(h), even for Pt/TmIG with comparable PMA, the MP-MR at low T is substantially larger than that at elevated T. This indicates that the enhancement of MP-MR cannot be fully explained by the increase in PMA alone. Instead, the strengthening of exchange coupling at low T is expected to play an important role, leading to a larger ferromagnetism in Pt.

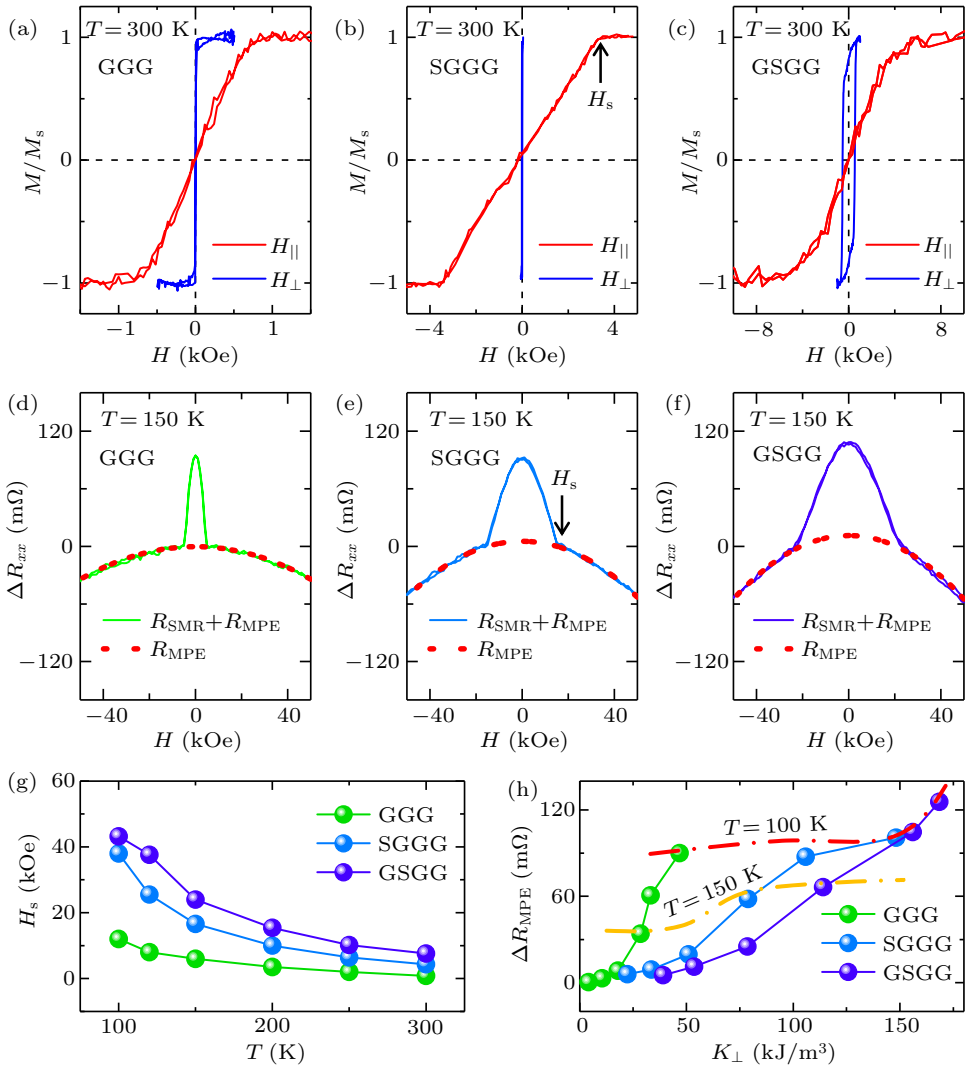


Fig. 5. PMA enhancement of MP-MR. (a)–(c) M–H hysteresis loops measured at 300 K from the TmIG/GGG(111), TmIG/SGGG(111), and TmIG/GSGG(111) films measured with both $H_\parallel$ and $H_\perp$. (d)–(f) The experimental data of ΔR_{xx} for Pt/TmIG on different substrates as a function of the H at 150 K and the fitting curve with the quadratic functions. (g) The H_s–T curves of Pt/TmIG on different substrates. (h) ΔR^*_{MPE} values for Pt/TmIG on different substrates as functions of $K_\perp$, where $K_\perp = H_s \cdot M_s/2$.

3. Conclusions

We successfully identified an intriguing MR phenomenon induced by the MPE in the Pt/TmIG interface, which we refer to as MP-MR. It is an electrical signal directly correlated with the itinerant ferromagnetism induced by the MPE at the Pt/TmIG interface. The existence of this signal has been unambiguously confirmed by introducing a Cu interlayer and quantitative data analysis, which also allows it to be clearly distinguished from the SMR signal. By employing TmIG films with enhanced PMA, we have confirmed that optimizing PMA to enhance MPE represents a viable strategy for improving the MP-MR. Our findings provide a new strategy for modulating material properties through MPE, demonstrating significant potential for advancing their applications in spintronic devices.

Appendix A: Experimental details

Film growth: We prepared the $Tm_3Fe_5O_{12}$ (TmIG) polycrystalline targets by first sintering a mixture of stoichiometric amounts of Fe_2O_3 and Tm_2O_3 at 1300 °C for 24 h and then grinding and pressing them into pellets. Using this polycrystalline target, the TmIG films were grown on (111)-oriented $Gd_3Ga_5O_{12}$ [GGG(111)], $Gd_{2.6}Ca_{0.4}Ga_{4.1}Mg_{0.25}Zr_{0.65}O_{12}$ [SGGG(111)], and $Gd_3Sc_2Ga_3O_{12}$ [GSGG(111)] substrates by pulsed laser deposition (PLD). In the PLD chamber, the substrate–target distance is approximately 5.5 cm. To ensure good thermal contact, the substrates were attached to the sample holder with conductive silver paste. During the film deposition, we kept the substrate temperature, laser spot size, laser fluence, and laser repetition rate at 750 °C, 1×3 mm^2, 2.0 J/cm^2, and 5 Hz, respectively. After deposition, we *in situ* annealed the as-grown film at the same conditions for 10 min and then cooled the film down to room temperature with a cooling rate of 50 °C/min. Then, we deposited a Pt layer on top of TmIG using PLD *in situ* at room temperature. During the film deposition, we kept high vacuum conditions and a 10 Hz laser repetition rate.

Structural characterization (XRD): The epitaxial quality of the TmIG films was analyzed using a high-resolution x-ray diffractometer (PANalytical Empyrean x-ray diffractometer, Cu $K\alpha 1$ radiation) with both the 2θ–ω linear scan. The thicknesses of the TmIG films were determined by fitting the Laue fringes.

Magnetic and electrical characterizations: The magnetic field-dependent magnetization (M–H) curves were measured using a vibrating sample magnetometer (VSM-SQUID, Quantum Design). During the M–H measurements, we placed the films in different geometries so that the H applied field was aligned along the film normal or in-plane. The longitudinal and transverse resistances were measured using a physical properties measurement system (PPMS, Quantum Design).

Acknowledgements

This work is supported by the National Basic Research Program of China (Grant No. 2023YFA1406404), the National Natural Science Foundation of China (Grant Nos. 12504152, 52572144, 12304153, 12374094, 12074365, 11974326, and 12274120), the Fundamental Research Funds for the Central Universities (Grant No. WK9990000158), CAS Project for Young Scientists in Basic Research (Grant No. YSBR-084), Innovation Program for Quantum Science and Technology (Grant No. 2024ZD0301300), the China Postdoctoral Science Foundation (Grant No. 2024M763130), the China Postdoctoral Science Foundation - Anhui Joint Support Program (Grant No. 2024T007AH), Anhui Provincial Natural Science Foundation (Grant No. 2308085MA15). The authors would like to thank the Information Science Laboratory Center for the hardware/software services and the USTC Center for Micro and Nanoscale Research and Fabrication for sample fabrication.

References

[1] Uchida K, Takahashi S, Harii K, Ieda J, Koshibae W, Ando K, Maekawa S and Saitoh E 2008 *Nature* **455** 778
[2] Uchida K, Xiao J, Adachi H, Ohe J, Takahashi S, Ieda J, Ota T, Kajiwara Y, Umezawa H, Kawai H, Bauer G E, Maekawa S and Saitoh E 2010 *Nat. Mater.* **9** 894
[3] Cornelissen L J, Liu J, Duine R A, Youssef J B, van Wees B J 2015 *Nat. Phys.* **11** 1022
[4] Sinova J, Valenzuela S O, Wunderlich J, Back C H and Jungwirth T 2015 *Rev. Mod. Phys.* **87** 1213
[5] Liu G, Wang X G, Luan Z Z, Zhou L F, Xia S Y, Yang B, Tian Y Z, Guo G H, Du J and Wu D 2021 *Phys. Rev. Lett.* **127** 207206
[6] Avci C O, Quindeau A, Pai C F, Mann M, Caretta L, Tang A S, Onbasli M C, Ross C A and Beach G S 2017 *Nat. Mater.* **16** 309
[7] Kobs A, Heße S, Kreuzpaintner W, Winkler G, Lott D, Weinberger P, Schreyer A and Oepen H P 2011 *Phys. Rev. Lett.* **106** 217207
[8] Ding Z, Chen B L, Liang J H, Zhu J, Li J X and Wu Y Z 2014 *Phys. Rev. B* **90** 134424
[9] Lang M, Montazeri M, Onbasli M C, Kou X, Fan Y, Upadhyaya P, Yao K, Liu F, Jiang Y, Jiang W, Wong K L, Yu G, Tang J, Nie T, He L, Schwartz R N, Wang Y, Ross C A and Wang K L 2014 *Nano Lett.* **14** 3459
[10] Wang Z, Tang C, Sachs R, Barlas Y and Shi J 2015 *Phys. Rev. Lett.* **114** 016603
[11] Tang C, Chang C Z, Zhao G, Liu Y, Jiang Z, Liu C X, McCartney M R, Smith D J, Chen T, Moodera J S and Shi J 2017 *Sci. Adv.* **3** e1700307
[12] Yang S R, Fanchiang Y T, Chen C C, Tseng C C, Liu Y C, Guo M X, Hong M, Lee S F and Kwo J 2019 *Phys. Rev. B* **100** 045138
[13] Wang Y, Mambakkam S V, Huang Y X, Wang Y, Ji Y, Xiao C, Yang S A, Law S A and Xiao J Q 2022 *Phys. Rev. B* **106** 155408
[14] Hu J, Han Y, Chi X, Omar G J, Al Ezzi M M E, Gou J, Yu X, Andrivo R, Watanabe K, Taniguchi T, Wee A T S, Qiao Z and Ariando A 2024 *Adv. Mater.* **36** 2305763
[15] Liang X, Zhu Y, Peng B, Deng L, Xie J, Lu H, Wu M and Bi L 2016 *ACS Appl. Mater. Interfaces* **8** 8175
[16] Huang S Y, Fan X, Qu D, Chen Y P, Wang W G, Wu J, Chen T Y, Xiao J Q and Chien C L 2012 *Phys. Rev. Lett.* **109** 107204
[17] Lin T, Tang C, Alyahayaei H M and Shi J 2014 *Phys. Rev. Lett.* **113** 037203
[18] Miao B F, Huang S Y, Qu D and Chien C L 2014 *Phys. Rev. Lett.* **112** 236601
[19] Huang S Y, Wang W G, Lee S F, Kwo J and Chien C L 2011 *Phys. Rev. Lett.* **107** 216604
[20] Qu D, Huang S Y, Hu J, Wu R and Chien C L 2013 *Phys. Rev. Lett.* **110** 067206
[21] Geprägs S, Meyer S, Altmannshofer S, Opel M, Wilhelm F, Rogalev A, Gross R and Goennenwein S T B 2012 *Appl. Phys. Lett.* **101** 1834
[22] Lu Y M, Choi Y, Ortega C M, Cheng X M, Cai J W, Huang S Y, Sun L and Chien C L 2013 *Phys. Rev. Lett.* **110** 147207
[23] Ding S, Ross A, Go D, Baldrati L, Ren Z, Freimuth F, Becker S, Kammerbauer F, Yang J, Jakob G, Mokrousov Y and Klaui M 2020 *Phys. Rev. Lett.* **125** 177201
[24] Avci C O, Rosenberg E, Caretta L, Büttner F, Mann M, Marcus C, Bono D, Ross C A and Beach G S D 2019 *Nat. Nanotechnol.* **14** 561
[25] Caretta L, Rosenberg E, Büttner F, Fakhrul T, Gargiani P, Valvidares M, Chen Z, Reddy P, Muller D A, Ross C A and Beach G S D 2020 *Nat. Commun.* **11** 1090
[26] Ding S, Ross A, Lebrun R, Becker S, Lee K, Boventer I, Das S, Kurokawa Y, Gupta S, Yang J, Jakob G and Kläui M 2019 *Phys. Rev. B* **100** 100406
[27] Shao Q, Liu Y, Yu G, Kim S K, Che X, Tang C, He Q L, Tserkovnyak Y, Shi J and Wang K L 2019 *Nat. Electron.* **2** 182
[28] Lee A J, Ahmed A S, Flores J, Guo S, Wang B, Bagues N, McComb D W and Yang F 2020 *Phys. Rev. Lett.* **124** 107201
[29] Ahmed A S, Lee A J, Bagues N, McCullian B A, Thabt A M A, Perrine A, Wu P K, Rowland J R, Randeria M, Hammel P C, McComb D W and Yang F 2019 *Nano Lett.* **19** 5683

[30] Tang C, Sellappan P, Liu Y, Xu Y, Garay J E and Shi J 2016 *Phys. Rev. B* **94** 140403

[31] Shao Q, Grutter A, Liu Y, Yu G, Yang C Y, Gilbert D A, Arenholz E, Shafer P, Che X, Tang C, Aldosary M, Navabi A, He Q L, Kirby B J, Shi J and Wang K L 2019 *Phys. Rev. B* **99** 104401

[32] Ding S, Liang Z, Yun C, Wu R, Xue M, Lin Z, Ross A, Becker S, Yang W, Ma X, Chen D, Sun K, Jakob G, Kläui M and Yang J 2021 *Phys. Rev. B* **104** 224410

[33] Liang Z, Lu J, Yang S, Fang Z, Yan Y, Wang Q, Li P, Fan M and Wang L 2024 *Adv. Funct. Mater.* **34** 2315147

[34] Nakamoto R, Xu B, Xu C, Xu H and Bellaiche L 2017 *Phys. Rev. B* **95** 024434

[35] Bauer J J, Rosenberg E R, Kundu S, Mkhoyan K A, Quarterman P, Grutter A J, Kirby B J, Borchers J A and Ross C A 2020 *Adv. Electron. Mater.* **6** 1900820

[36] Li Y, Zheng D, Fang B, Liu C, Zhang C, Chen A, Ma Y, Shen K, Liu H, Manchon A and Zhang X 2022 *Adv. Mater.* **34** 2200019

[37] Geller S, Remeika J P, Sherwood R C, Williams H J and Espinosa G P 1965 *Phys. Rev.* **137** A1034

[38] Bai H, Zhou H A, Li W, Xu T, Wang L, Gargiani P, Valvidares M and Jiang W 2025 *Phys. Rev. Appl.* **23** 044062

[39] Nakayama H, Althammer M, Chen Y T, Uchida K, Kajiwara Y, Kikuchi D, Ohtani T, Geprägs S, Opel M, Takahashi S, Gross R, Bauer G E W, Goennenwein S T B and Saitoh E 2013 *Phys. Rev. Lett.* **110** 206601

[40] Guo C Y, Wan C H, He W Q, Zhao M K, Yan Z R, Xing Y W, Wang X, Tang P, Liu Y Z, Zhang S, Liu Y W and Han X F 2020 *Nat. Electron.* **3** 304

[41] Hou D, Qiu Z, Barker J, Sato K, Yamamoto K, Vélez S, Gomez-Perez J M, Hueso L E, Casanova F and Saitoh E 2017 *Phys. Rev. Lett.* **118** 147202

[42] Zhou L, Song H, Liu K, Luan Z, Wang P, Sun L, Jiang S, Xiang H, Chen Y, Du J, Ding H, Xia K, Xiao J and Wu D 2018 *Sci. Adv.* **4** eaao3318

[43] Marmion S R, Ali M, McLaren M, Williams D A and Hickey B J 2014 *Phys. Rev. B* **89** 220404

[44] Shimizu S, Takahashi K S, Hatano T, Kawasaki M, Tokura Y and Iwasa Y 2013 *Phys. Rev. Lett.* **111** 216803

[45] Dugato D A, Brandão J, Béron F, Cezar J C, Denardin J C and Pasa A A 2023 *J. Magn. Magn. Mater.* **566** 170305

[46] Zheng X, Liu Y, Zhang H, Wang L, Chen X and Li W 2025 *Appl. Surf. Sci.* **680** 161394

[47] Moriya T and Kawabata A 1973 *J. Phys. Soc. Jpn.* **34** 639

[48] Negishi H, Yamada H, Yuri K, Sasaki M and Inoue M 1997 *Phys. Rev. B* **56** 11144

[49] Ohkawa F J 2002 *Phys. Rev. B* **65** 174424

[50] Xu Z, Liu Q, Ji Y, Li X, Li J, Wang J and Chen L 2022 *ACS Appl. Mater. Interfaces* **14** 16791

[51] Song Y, Lasinger K, Tang H, Li J, Beach G S D and Ross C A 2024 *Small* **20** 2407381